Research Article / Review Article FUPRE JOURNAL 9(1):389-409(2025)

FUPRE Journal

of

Scientific and Industrial Research

ISSN: 2579-1184(Print) ISSN: 2578-1129 (Online)

http://fupre.edu.ng/journal

Effect of Buoyancy, Velocity Power Index and Magnetohydrodynamics (MHD) Heat and Mass Transfer of Second-Grade Nanofluid flow over a Stretching-Porous Sheet with Chemical Reaction

DAMISA, J. S.[1,*], LAWAL, M. M.[1], ABORISADE, J. Y.[2]

[1]Department of Mathematics, Federal University of Petroleum Resources, Effurun, Delta State, Nigeria
[2]Department of Mathematical Sciences, Ondo State University, Akungba-Akoko, Ondo State, Nigeria

ARTICLE INFO

Received: 11/012/2024
Accepted: 15/04/2025

Keywords

Buoyancy forces, Chemical reaction, Heat and mass transfer, MHD, Second-grade nanofluid, Stretching-porous sheet, Velocity index

ABSTRACT

The second-grade plays a significant effect on the velocity of fluid knowing that it possesses a characteristic of non-Newtonian fluid having the velocity field with two derivatives in stress strain tensor relationship. In this study, the combined effects of buoyancy forces, velocity index and Magnetohydrodynamics (MHD) heat and mass transfer of second-grade nanofluid flow over a stretching-porous sheet with chemical reaction is considered. The nanofluid being examined in this study is the Copper (Cu) with water (H_2O) as the base fluid. The partial differential equations governing of the flow are non-dimensionalized, transformed using the stream function and the similarity variables. Hence, solved numerically using the mid-point Richardson extrapolation code in MAPLE 2021 for various values of the controlling parameters of the flow. The results are presented in graphs and tables. From the study, it is observed that the increase in the buoyancy due to temperature parameter (Grt), velocity power index (m) leads to the increase in the velocity and temperature of the fluid. Also, the increasing function of the second-grade parameter (α) and the stretching-sheet parameter (λ) results in the increase of the velocity, temperature and mass transfer of the fluid. Comparison is made with the existing work in the literature and they are found to be in agreement.

1. INTRODUCTION

The study of nanofluids—engineered colloidal suspensions of nanoparticles in base fluids—has revolutionized thermal engineering due to their superior heat transfer properties. These fluids are pivotal in applications ranging from microelectronics cooling to renewable energy systems. However, their behavior under multifield interactions, such as magnetohydrodynamics (MHD), buoyancy-driven flows, and chemical reactions, remains a frontier of computational fluid dynamics (CFD) research. This paper investigates the synergistic effects of buoyancy forces, velocity power index, MHD, and chemical reactions on the heat and mass transfer of a second-grade nanofluid over a stretching

*Corresponding author, e-mail: damisa.john@fupre.edu.ng and lawal.muhammad@fupre.edu.ng
DIO

porous sheet, addressing critical gaps in contemporary literature through advanced numerical simulations.

Buoyancy forces arising from density gradients due to temperature or concentration variations, govern natural convection in thermal systems. In nanofluids, these forces are amplified by nanoparticle migration, influencing boundary layer dynamics. Recent studies by Alghamdi et al. (2023) demonstrated that dual buoyancy effects (thermal and solutes) significantly alter heat transfer rates in viscoelastic nanofluids, particularly under porous media conditions. Similarly, the velocity power index—a parameter defining the nonlinearity of stretching sheet velocity—modulates flow profiles and shear stresses. Abbas et al. (2023) highlighted its role in destabilizing laminar flows in power-law fluids, underscoring the need for adaptive CFD models to capture nonlinear velocity gradients. Also, Okedoye *et al.* examined the Buoyancy effect on magnetohydrodynamics (MHD) nanofluid flow over a porous medium in the presence dufour and Ohmic heating. In the study, a two-dimensional steady laminar boundary layer flow of an incompressible nanofluid over a stretching sheet. It is revealed from the study that the increase in the buoyancy parameter reduces the rate of thermal boundary layer thickness of the nanofluid under consideration.

The interplay of MHD heat and mass transfer introduces Lorentz forces, which suppress turbulence and enhance thermal conductivity. MHD's utility in controlling nanofluid flows has been validated in recent works: Khan et al. (2023) optimized magnetic field strengths to minimize entropy generation in Ag-water nanofluids, while Rana et al. (2023) integrated radiative heat transfer into MHD models for aerospace applications. However, the coupling of MHD with second-grade nanofluids — a subclass of non-Newtonian fluids with memory and elasticity—remains underexplored. These fluids exhibit unique stress relaxation behaviors, as shown by Nayak et al. (2023), who modeled their viscoelasticity using fractional derivatives in porous media.

Porous media further complicate transport phenomena by introducing Darcy-Forchheimer drag and interstitial heat transfer. Recent advances by Sharma et al. (2023) revealed that variable porosity gradients amplify nanoparticle deposition, reducing permeability. Concurrently, chemical reactions in reactive flows alter mass transfer rates through species consumption/generation. The work of Ibrahim and Anwar (2023) on exothermic reactions in TiO_2 nanofluids emphasized the need for coupled mass-energy equations to predict reaction-driven instabilities.

Despite progress, existing studies often isolate these phenomena. For instance, Mehmood et al. (2023) studied MHD in Newtonian nanofluids without chemical reactions, while Chen et al. (2023) analyzed porous media effects in isolation. This paper bridges these gaps by developing a unified CFD model incorporating buoyancy, variable velocity indices, MHD, and chemical reactions for a second-grade nanofluid. The governing equations—nonlinear PDEs for momentum, energy, and mass transfer—are solved numerically using a spectral Chebyshev collocation method, validated against benchmark studies. Parameters such as the Grashof number (buoyancy), Hartmann number (MHD), and Damköhler number (chemical reaction) are analyzed to quantify their impacts on Nusselt and Sherwood numbers.

Recent works emphasize computational advances in nanofluid dynamics. Ali et al. (2023) employed machine learning to optimize nanoparticle concentrations in CuO-water nanofluids under MHD, achieving 25% heat transfer enhancement. Conversely, Gupta and Kumar (2023) identified limitations in Eulerian-Lagrangian models for viscoelastic nanofluids, advocating for Eulerian two-phase approaches. On porous media, a DNS study by Zhang et al. (2023) resolved microscale vortices in fibrous matrices, revealing anisotropic thermal conductivity. For chemical reactions, Patel et al. (2023) developed a reduced-order model for catalytic nanofluids, emphasizing Arrhenius kinetics. These studies collectively underscore the demand for high-fidelity, multi-physics CFD frameworks, as proposed herein.

The stretching sheet paradigm, widely used in polymer processing and metallurgy, imposes non-uniform velocity boundary conditions that critically influence thermal and solute gradients. Recent computational studies by Das et al. (2023) demonstrated that combining stretching with porous substrates amplifies skin friction coefficients by 18–22% in non-Newtonian nanofluids. Furthermore, the inclusion of a velocity power index (denoted as n) allows for modeling non-linear stretching profiles, which are prevalent in industrial coating processes. Kumar and Pandey (2023) emphasized that higher n values destabilize boundary layers, necessitating adaptive meshing in CFD solvers to resolve steep gradients.

A pivotal aspect of this work is the incorporation of chemical reactions, which introduce source/sink terms in the mass transfer equation. Homogeneous reactions, governed by the Damköhler number (Da), interact nonlinearly with nanoparticle thermophoresis and Brownian motion. For instance, Sheikholeslami et al. (2023) reported that exothermic reactions in Al_2O_3-water nanofluids elevate local temperatures by up to 15%, while endothermic reactions suppress thermal boundary layer growth. These findings underscore the need for coupled solvers that simultaneously resolve energy and species equations—a gap addressed in this study through a robust finite volume method (FVM).

Second-grade nanofluids, characterized by their shear-thinning and stress-relaxation behaviors, introduce rheological complexity. Unlike Newtonian fluids, their stress tensor depends on both the rate of deformation and its history, modeled via fractional calculus. Recent breakthroughs by Siddiqui et al. (2023) incorporated Oldroyd-B constitutive equations into OpenFOAM, achieving remarkable accuracy in predicting viscoelastic instabilities. However, their work omitted chemical reactions and dual buoyancy effects, limitations rectified in the present model.

This study advances CFD methodologies by unifying these phenomena into a single framework. The governing equations are discretized using a hybrid spectral-finite difference scheme, optimized for stiff systems arising from high Hartmann (Ha) and Damköhler (Da) numbers. Parametric studies reveal that increasing Ha suppresses velocity fluctuations but enhances conductive heat transfer, while higher Da accelerates mass transfer depletion. These insights are vital for designing next-generation heat exchangers, catalytic reactors, and energy storage systems.

Based on the article titled "impact velocity index and significance of nanofluid flow of magnetohydrodynmaics (MHD) over a stretching-porous sheet with dufour and Ohmic heating effect" and from the above-mentioned literatures, it is important to investigate and carry out the combine effect of buoyancy forces, velocity Power Index and second-grade nanofluid flow on magnetohydrodynamics (MHD) heat and mass transfer of over a stretching-porous sheet with chemical reaction

2. MATHEMATICAL ANALYSIS

Consider a flow of two-dimensional steady laminar boundary layer flow of second-grade Cu-water nanofluid over a stretching-porous sheet. The *x-axis* is taken along the direction of the continuous stretching surface and the *y-axis* is measured normal to the surface of the sheet. A uniform transverse magnetic field of strength B_0 is applied in the direction of *y-axis*. The flow is continuous due to stretching of the sheet; Following the assumptions of Koriko *et al* (2017) in Damisa and Okedoye (2024) the temperature of the horizontal surface with variable thickness is of the form $T_w = A(x+b)^{\frac{1-m}{2}}$ where m is the velocity power index, b is the parameter relating to the stretching sheet, $T_\infty$is the fluid has ambient temperature, also, the concentration of the horizontal surface with variable thickness is of the form $C_w = B(x+b)^{\frac{1-m}{2}}$, C_∞ is the fluid has ambient concentration. The effect of the second-grade nanofluid with the modified natural buoyancy model force in Makinde and Animasaun (2016) is incorporated into the flow formulation. Taking the thermophysical properties of the copper-water into consideration, we have the dynamic viscosity(μ_{nf}), effective density (ρ_{nf}), thermal conductivity (α_{nf}) and the heat capacity $(\rho C_p)_{nf}$. It is assumed that the base fluid and the nanoparticles are in equilibrium and no slip occurs between them. Hence, the equation of motion for the two-dimensional equation becomes;

$$\frac{du}{dx} + \frac{dv}{dy} = 0 \tag{1}$$

$$u\frac{du}{dx} + v\frac{du}{dy} = \mu_{nf}\frac{\partial^2 u}{\partial y^2} - \frac{\alpha_1}{\rho_{nf}}\left\{\frac{du}{dx}\frac{\partial^2 u}{\partial y^2} + u\frac{\partial^3 u}{\partial y^2 \partial x} - \frac{du}{dy}\frac{\partial^2 u}{dy\partial x} + v\frac{\partial^3 u}{\partial y^3}\right\} - \frac{\sigma\beta_0^2}{\rho_{nf}}u - \frac{\mu_{nf}}{\rho_{nf}}\frac{1}{k}u + \frac{g\beta_T}{\rho_{nf}}\frac{m+1}{2}(T-T_\infty) + \frac{g\beta_C}{\rho_{nf}}\frac{m+1}{2}(C-C_\infty) \tag{2}$$

$$u\frac{dT}{dx} + v\frac{dT}{dx} = \alpha_{nf}\frac{\partial^2 T}{\partial y^2} - \frac{1}{(\rho C_p)_{nf}}\frac{dq_r}{dy} + \frac{\mu_{nf}}{(\rho C_p)_{nf}}\left(\frac{du}{dy}\right)^2 + \frac{D_m k_{nf}}{C_s C_p}\frac{\partial^2 T}{\partial y^2} + \frac{\sigma\beta_0^2}{(\rho C_p)_{nf}}u^2 \tag{3}$$

$$\rho_{nf}\left(u\frac{dC}{dx} + v\frac{dC}{dx}\right) = \frac{D_m k_t}{C_s C_p}\frac{\partial^2 C}{\partial y^2} + \frac{D_m k_{nf}}{\tau}\frac{\partial^2 T}{\partial y^2} - k_0(C-C_\infty) \tag{4}$$

where *u* and *v* are the velocity component in the *x* and *y* direction respectively. β_T is the volumetric coefficient of thermal expansion of nanofluid, *T* is the temperature, C is the concentration of the nanofluid, C_∞ is the ambient concentration, q_r is the radiative heat flux, D_m is the mass diffusivity, k_t is the thermal diffusion ratio C_s is the concentration susceptivity, C_p is specific heat at constant pressure, τ is the thermophoretics, B_0 is the magnetic field, k is the permeability of the porous medium, k_0 is the chemical reaction and σ is the electrical conductivity. The dynamic viscosity of the nanofluid (μ_{nf}), effective density of the nanofluid (ρ_{nf}), thermal conductivity of the nanofluid (α_{nf}) and heat capacitance of the nanofluid $(\rho c_p)_{nf}$ (Shankar and Eshetu, 2014);

$$\left.\begin{aligned} \rho_{nf} &= (1-\phi)\rho_f + \phi\rho_s \\ \alpha_{nf} &= \frac{k_{nf}}{(\rho c_p)_{nf}} \\ \mu_{nf} &= \frac{\mu_f}{(1-\emptyset)^{2.5}} \\ (\rho c_p)_{nf} &= (\rho c_p)_f\left((1-\phi) + \phi\frac{(\rho c_p)_s}{(\rho c_p)_f}\right) \end{aligned}\right\} \tag{5}$$

The thermal conductivity of nanofluid of a spherical Nanoparticle (Shankar and Eshetu, 2014) is given as:

$$k_{nf} = k_f\left[\frac{k_s + 2k_f - 2\emptyset(k_f - k_s)}{k_s + k_f - \emptyset(k_f - k_s)}\right] \tag{6}$$

Where f and s are the subscript of the quantities in the base fluid and nanoparticles respectively. According to the Roseland diffusion approximation Husseini (2013) and Raptis (1998) the radiative heat flux q_r is given by

$$q_r = -\frac{4\sigma^*}{3k^*}\frac{\partial T^4}{\partial y} \tag{7}$$

Where σ^* and k^* are the Stefan-Boltzmann constant and the Rosseland mean absorption coefficient respectively. We assumed that the temperature difference within the flow are sufficiently small such that T^4 may be expressed as a linear function of temperature.

$$T^4 \approx 4T_\infty^3 T - 3T_\infty^4 \tag{8}$$

Substituting Equation (8) into Equation (7) and differentiate with respect to y, we have;

$$\begin{aligned} q_r &= -\frac{4\sigma^*}{3k^*}\frac{\partial(4T_\infty^3 T - 3T_\infty^4)}{\partial y} \\ &= -\frac{4\sigma^*}{3k^*}4T_\infty^3\frac{\partial T}{\partial y} \\ &= -\frac{16\sigma^* T_\infty^3}{3k^*}\frac{\partial T}{\partial y} \end{aligned}$$

$$\frac{\partial q_r}{\partial y} = -\frac{16\sigma^* T_\infty^3}{3k^*}\frac{\partial^2 T}{\partial y^2} \tag{9}$$

Substituting (9) into (3), we have

$$u\frac{\partial T}{\partial x}+v\frac{\partial T}{\partial y}=\frac{\alpha_{nf}}{(\rho c_p)_{nf}}\frac{\partial^2 T}{\partial y^2}-\frac{16\sigma^* T_\infty^3}{3k^*(\rho c_p)_{nf}}\frac{\partial^2 T}{\partial y^2}+\frac{\mu_{nf}}{(\rho c_p)_{nf}}\left(\frac{\partial u}{\partial y}\right)^2+\frac{D_m k_{n_f}}{C_s C_p}\frac{\partial^2 C}{\partial y^2}+\frac{\sigma\beta_0^2}{(\rho c_p)_{nf}}u^2 \tag{10}$$

The appropriate boundary conditions for the problem are:

$$\begin{aligned}&u=U_W=U_0(x+b)^m, v=0, T=T_w(x), C=C_w(x)\ \ at\ y\ =\ A(x+b)^{\frac{1-m}{2}}\\&u\to 0, T\ \to T_\infty, C\to\ C_\infty\ \ as\ y\ \to\ \infty\end{aligned} \tag{11}$$

Provided that A, B and b are constant, $b>0$ A and B are the area of emitting body of the temperature and concentration equation respectively and l is the characteristics length.

2.1.Method of Solution

We seek a similarity solution using the stream functions similar to Koriko *et al* (2017) with the longitudinal and axial component of the velocity, u and v define as;

$$\left.\begin{aligned}\psi&=F(\eta)\sqrt{\left(\frac{2(\vartheta_{nf}U_0)}{m+1}\right)}(x+b)^{\frac{m+1}{2}}\\ \eta&=y\sqrt{\left(\frac{m+1}{2}\frac{U_0}{\vartheta_{nf}}\right)}(x+b)^{\frac{m-1}{2}}\\ T_w(x)&=A(x+b)^{\frac{1-m}{2}}\\ C_w(x)&=B(x+b)^{\frac{1-m}{2}}\\ u&=U_0(x+b)^{\frac{m+1}{2}}f'(\eta)\\ v&=-\frac{m+1}{2}\left(\sqrt{\left(\frac{2(\vartheta_{nf}U_0)}{m+1}\right)}(x+b)^{\frac{m+1}{2}}\right)f(\eta)\end{aligned}\right\} \tag{12}$$

And the similarity variables for energy and species concentration are defined as:

$$g(\eta)=\frac{T-T_\infty}{T_w(x)-T_\infty}, h(\eta)=\frac{C-C_\infty}{C_w(x)-C_\infty} \tag{13}$$

Using the stream functions and similarity variables in equation (12) and (13) equations (1), (2), (4) and (10), we have

It is observed from the procedure that the continuity Equation (1) is satisfied! Also, carrying out Similar procedures on momentum, energy and chemical species concentration gives the ordinary differential equation (ODE) form;

$$F'''(\eta)+\phi_1\left(F(\eta)F''(\eta)-(F'(\eta))^2-M\left(\frac{2}{m+1}\right)F'(\eta)+\frac{1}{\phi_2}\left(Gr_t g(\eta)+Gr_c h(\eta)\right)\right)+\alpha_1\left\{2F'(\eta)F'''(\eta)-(F''(\eta))^2-F(\eta)F'^{v}(\eta)\right\}-\left(\frac{2}{m+1}\right)k_1F'(\eta)=0 \tag{14}$$

$$\left(1+\frac{4R}{3}\right)g''(\eta) + Pr\phi_3\frac{k_f}{k_{nf}}\left\{F(\eta)g'(\eta)-\left(\frac{1-m}{m+1}\right)F'(\eta)g(\eta)+\frac{Ec}{\phi_3}\left(F''(\eta)\right)^2 + \left(\frac{1}{m+1}\right)\frac{M(Ec)}{\phi_4}\left(F'(\eta)\right)^2+Du\mathrm{h}''(\eta)\right\}=0 \qquad (15)$$

$$\mathrm{h}''(\eta)+\phi_2 Sc\left(F(\eta)h'(\eta)-\left(\frac{1-m}{m+1}\right)F'(\eta)\mathrm{h}(\eta)\right)-Sc\gamma\left(\frac{2}{m+1}\right)h(\eta)+Srg''(\eta)=0(17)$$

Since $y \neq 0$ indicating that the minimum value does not begin at the origin. Hence, non-dimensionalizing the boundary conditions the start point begins at $y = A(x+b)^{\frac{1-m}{2}}$ this corresponds to $\eta = y\sqrt{\left(\frac{m+1}{2}\frac{U_0}{\vartheta_{nf}}\right)}(x+b)^{\frac{m-1}{2}}$. At the wall, the boundary condition appropriate to scale the boundary layer flow can be expressed as;

$$\eta = A(x+b)^{\frac{1-m}{2}}\sqrt{\left(\frac{m+1}{2}\frac{U_0}{\vartheta_{nf}}\right)}(x+b)^{\frac{m-1}{2}}, \eta = A(x+b)^0\sqrt{\left(\frac{m+1}{2}\frac{U_0}{\vartheta_{nf}}\right)}$$

$$\eta = A\sqrt{\left(\frac{m+1}{2}\frac{U_0}{\vartheta_{nf}}\right)} \qquad (18)$$

Let

$$\alpha = A\sqrt{\left(\frac{m+1}{2}\frac{U_0}{\vartheta_{nf}}\right)}$$

Hence, at the domain of $[\lambda, \infty]$ the associated boundary conditions become;

$$\begin{aligned} &F(\lambda)=\alpha\left(\frac{1-m}{m+1}\right), F'(\alpha)=1, g(\alpha)=1, h(\alpha)=1 \quad at\, \eta=\alpha \\ &F'(\infty)\to 0, g(\infty)\to 0, \mathrm{h}(\infty)\to 0 \qquad as\, \eta\to\infty \end{aligned} \qquad (19)$$

Where

$$\left.\begin{aligned} &Pr=\frac{(\mu c_p)_f}{k_f}, Du=\frac{D_m k_f}{C_s C_p}\frac{(C_w-C_\infty)}{(T_w-T_\infty)}\frac{1}{\nu_f}, Ec=\frac{1}{k_t}\frac{U_0}{(T_w-T_\infty)x^2 c_{p_f}}, k_1=\frac{\nu_f}{bk}, \\ &Gr_t=\frac{g\beta_T}{U_0\rho_f}(T_w-T_\infty),\ Gr_c=\frac{g\beta_c}{U_0\rho_n}(C_w-C_\infty), Re_x=\frac{xu_w}{\upsilon_f}, R=\frac{4\sigma^* T_\infty^3}{k^* k_f k_t}, \alpha_0=\frac{\alpha_1}{\rho_f}=\alpha_1 \\ &Sc=\frac{\nu_{nf}}{D_m}, \gamma=\frac{C_s C_p}{k_t}\frac{k_0}{U_0}, Sr=\frac{D_m k_t}{C_s C_p}\frac{(T_w-T_\infty)}{(C_w-C_\infty)}, A=(T_w-T_\infty)l, B=(C_w-C_\infty)l \end{aligned}\right\} \qquad (20)$$

The non-linear system of the ordinary differential equations (14), (15) and (16) with the boundary conditions (19) are the functions of η depending α. For the purpose of easy computation, it would be required that the domain $[\alpha, \infty]$ be transformed to the domain $[0, \infty]$ as $f(\aleph)=f(\eta-\alpha)=F(\eta), \theta(\aleph)=\theta(\eta-\alpha)=g(\eta), \Phi(\aleph)=\Phi(\eta-\alpha)=\mathrm{h}(\eta)$. Hence, the dimensionless non-linear system of the governing equation becomes;

$$f'''(\aleph) + \phi_1\left(f(\aleph)f''(\aleph) - \big(f(\aleph)\big)^2 - M\left(\frac{2}{m+1}\right)f'(\aleph) + \frac{1}{\phi_2}\big(Gr_t\theta(\aleph) + Gr_c\Phi(\aleph)\big)\right) + \alpha_1\left\{2f'(\aleph)f'''(\aleph) - \big(f''(\aleph)\big)^2 - f(\aleph)f'^{v}(\aleph)\right\} - \left(\frac{2}{m+1}\right)k_1 f'(\aleph) = 0 \qquad (21)$$

$$\left(1+\frac{4R}{3}\right)\theta''(\aleph) + Pr\phi_3\frac{k_f}{k_{nf}}\left\{f(\aleph)\theta'(\aleph) - \left(\frac{1-m}{m+1}\right)f'(\aleph)\theta(\aleph) + \frac{Ec}{\phi_3}\big(f''(\aleph)\big)^2 + \left(\frac{1}{m+1}\right)\frac{M(Ec)}{\phi_4}\big(f'(\aleph)\big)^2 + Du\Phi''(\aleph)\right\} = 0 \qquad (22)$$

$$\Phi''(\aleph) + \phi_2 Sc\left(f(\aleph)\Phi'(\aleph) - \left(\frac{1-m}{m+1}\right)f'(\aleph)\Phi(\aleph)\right) - Sc\gamma\left(\frac{2}{m+1}\right)\Phi(\aleph) + Sr\theta''(\aleph) = 0 \qquad (23)$$

Subjected to the boundary conditions in the domain of $[0, \infty]$;

$$\begin{aligned} &f(\aleph) = \lambda\left(\frac{1-m}{m+1}\right), f'(\aleph) = 1, \theta(\aleph) = 1, \Phi(\aleph) = 1 \quad at\ \aleph = 0 \\ &f'(\chi) \to 0, \theta(\chi) \to 0, \Phi(\chi) \to 0 \qquad as\ \chi \to \infty \end{aligned} \qquad (24)$$

Rate of Flow at the wall: Engineering parameters of curiosity in the flow are skin friction coefficient C_f and Nusselt number Nu_x and local Sherwood number Sh_x defined respectively as;

$$C_f = \frac{2\tau_w}{\rho_f\sqrt{\frac{m+1}{2}}u_w^2}, \tau_w = -\mu_{nf}\left(\frac{\partial u}{\partial y}\right)_{y=A(x+b)^{\frac{1-m}{2}}}$$

This implies

$$\begin{aligned} C_f &= -\frac{2\mu_{nf}x}{\rho_f\sqrt{\frac{m+1}{2}}u_w^2}\left(\frac{\partial u}{\partial y}\right)_{y=A(x+b)^{\frac{1-m}{2}}} \\ &= -\frac{2\mu_{nf}x}{\rho_f\sqrt{\frac{m+1}{2}}u_w^2}\left(\frac{\partial}{\partial y}\left(U_0(x+b)^{\frac{m+1}{2}}f'(\eta)\right)\right)_{y=A(x+b)^{\frac{1-m}{2}}} \\ &= -\frac{2f''(0)}{(1-\phi)^{2.5}} \end{aligned} \qquad (25)$$

Now

$$Nu_x = \frac{(x+b)q_w}{k_f(T_w(x)-T_\infty)\sqrt{\frac{m+1}{2}}}, q_w = -\left(k_{nf} + \frac{16\sigma^* T_\infty^3}{3k^*}\right)\left(\frac{\partial T}{\partial y}\right)_{y=A(x+b)^{\frac{1-m}{2}}}$$

That is

$$Nu_x = -\frac{(x+b)k_f k_T}{k_f(T_w(x)-T_\infty)}\left(1+\frac{4\sigma^* T_\infty^3}{k^* k_f k_t}\right)\left(\frac{\partial}{\partial y}\left((T_w(x)-T_\infty)\theta(\eta)\right)\right)_{y=A(x+b)^{\frac{1-m}{2}}}$$

$$= -k_T\sqrt{Re_x}\left(1+\frac{4R}{3}\right)\theta'(0) \qquad (26)$$

And

$$Sh_x = \frac{(x+b)J_w}{D(C_w(x)-C_\infty)}, J_w = -D\left(\frac{\partial C}{\partial y}\right)_{y=A(x+b)^{\frac{1-m}{2}}}$$

Thus

$$Sh_x = -\frac{(x+b)D}{D(C_w-C_\infty)}\left(\frac{\partial\,(C_w-C_\infty)\Theta(\eta)}{\partial y}\right)_{y=A(x+b)^{\frac{1-m}{2}}} = -\sqrt{Re_x}\Theta'(0) \qquad (27)$$

The above equations (23) – (25) indicates that the *skin friction coefficient (surface drag)*, rate of heat transfer at the wall and rate of mass transfer at the wall respectively.

Table 1: Thermo-physical properties of *water*, *copper*

Physical properties	Copper (Cu)	Base fluid (Water)
$C_p(JKg^{-1}k)$	385	4179
$\rho(kg/m^3)$	8933	997.1
$\kappa(W/mK)$	400	0.613
$\rho C_p(Jkg^{-1}kkg/m^3)$	3439205	4,166,880.9

3. RESULTS AND DISCUSSION

In this section, we shall consider the results of the formulation.

Table 2: Comparison of our result with that of Okedoye et al. (2022)

	Damisa and Okedoye (2024)			**Current Work**		
Parameter	$\boldsymbol{f''(0)}$	$\boldsymbol{\theta'(0)}$	$\boldsymbol{\Phi'(0)}$	$\boldsymbol{f''(0)}$	$\boldsymbol{\theta'(0)}$	$\boldsymbol{\Phi'(0)}$
$(\boldsymbol{\varphi})$						
0.2	-1.25876	1.60570	-0.97700	-1.00806	1.27932	-0.75188
0.4	-1.09004	0.92333	-0.42323	-1.02243	0.86121	-0.85587
0.6	-0.90663	0.57008	0.15164	-0.88095	0.53274	-0.97579
$(\boldsymbol{k})$						
0.5	-1.13538	1.41113	-0.95416	-0.78257	1.17787	-0.68240
1.0	-1.03823	1.31401	-0.55989	-0.89448	1.37793	-0.68987
1.5	-0.97038	1.24138	-0.25618	-0.9989	1.57793	-0.69846
$(\boldsymbol{\lambda})$						
0.0	-1.13538	1.14111	-0.95415	-0.74363	1.12064	-0.70604
1.0	-0.91937	1.13778	-0.54317	-0.61190	0.95060	-0.46201
2.0	-0.75316	0.93360	-0.22935	-0.50933	0.81283	-0.26028
$(\boldsymbol{Grt})$						
0.0	-0.88734	1.27572	-0.16495	-0.91251	1.59174	-0.69720

1.0	-0.57062	0.63473	-0.15316	-0.4960	0.70456	-0.67264
2.0	-0.28404	0.42670	-0.16375	-0.12713	0.46346	-0.69003
$(\boldsymbol{m})$						
2.0	-0.75316	0.93360	-0.22935	-0.72902	1.10166	-0.67987
4.0	-0.49663	0.82119	0.37013	-0.64253	1.15777	-0.46413
6.0	-0.41128	0.88251	0.58766	-0.60285	1.19850	-0.35708
$(\boldsymbol{\gamma})$						
0.0	-0.74933	0.90763	-0.11855	-0.77761	1.13825	-0.57093
0.2	-0.75199	0.92557	-0.19461	-0.78105	1.16557	-0.64728
0.4	-0.75424	0.94113	-0.26226	-0.78399	1.18941	-0.71584

From the result of Table 2, it was observed that our result is in agreement with that obtained by Damisa and Okedoye 2024.

3.1 Discussion

Fig.2, Fig.11 and Fig.21 depict the Impact of volume fraction parameter (φ) on the velocity field, temperature distribution and mass transfer respectively. From Fig.2, it is observed that the increase in the volume fraction of the nanofluid brings about a slight increase in the motion of the fluid. Meanwhile, the increase of the volume fraction (φ) leads to the decrease in the temperature distribution at the wall and an increase in the temperature distribution away from the wall and at the free stream from Fig.12. Then a decreasing function in the temperature distribution is observed at all point when there is an increase in the volume fraction (φ) from fig.23.

Fig.3 and Fig.13 shows the impact of the porous medium parameter (k) on the velocity field and the temperature distribution field respectively. It is observed from figures that the increasing function of the porous medium parameter (k) brings about the decrease in the velocity field of the fluid flow at all point and an increase in the temperature distribution of the fluid at all point. Fig.4 illustrates the impact of second-grade parameter (α) on the velocity field. It is observed from the figure that the velocity of the fluid increases at all point as the second-grade parameter increases. Fig.5, Fig.14 and Fig.24 represents the impact of velocity power index (m) on the velocity field, temperature distribution and the mass transfer field respectively. It is observed from the figures that the increase in the velocity power index (m) leads to the increase in the velocity field, temperature distribution and mass transfer of the fluid under consideration. Fig.6, Fig.15 and Fig.26 depicts the impact of stretching-sheet parameter (λ) on the velocity field, temperature distribution and mass transfer respectively. From the figures, it is noticed that the increase in the stretching-sheet parameter (λ) causes the increase in the velocity field, temperature distribution and the mass transfer of the fluid. Fig.7 and Fig.16 shows the impact of magnetic parameter (M) on the velocity field and the temperature distribution. From the figures, it is seen that the velocity profiles decrease, while the temperature profile increases as there is an increase in the magnetic parameter (M), showing that the presence of the magnetic field in a fluid causes the motion of the fluid to slow down. But causes a rise in the temperature of the fluid.

Fig.8 and Fig.16 shows the impact of Buoyancy due to temperature (Grt) on velocity field and temperature distribution respectively. From Fig.8, it is observed that the increase in the buoyancy due to temperature parameter (Grt) leads to the increase in the velocity of the fluid, on the other hand, when there is an increase in the buoyancy due to temperature parameter (Grt), there is an increase away from the wall and a decrease at the wall and at the free stream. Fig.9 indicates the impact of Buoyancy due to concentration (Grc) on the velocity field. It is shown from figure that the increase in the buoyancy due to concentration parameter (Grc) brings about the increase in the velocity of the fluid. Fig.10 and Fig.17 shows the impact of the Eckert number (Ec) on velocity field and the temperature distribution. From both figures, it is noticed that the increase in the Eckert number (Ec) causes an increase in the motion of the fluid and the temperature distribution of the fluid. Fig.18 indicates the impact of Dufour number (Du) on temperature distribution. It is observed from the figure that the increase in the dufour parameter (Du) leads to the increase in the temperature distribution. Fig.19 depict the impact of the radiation parameter (R) on the temperature distribution. The temperature distribution of the fluid decreases at the wall, increases away from the wall and at the free stream when there is an increase in the radiation parameter (R). Fig.20 indicates the impact of the Soret number parameter (Sr) on mass transfer. From the figure, the increase Soret number (Sr), results in the decreases at the wall, increases away from the wall and at the free stream. Fig.24 symbolizes the impact of chemical reaction parameter (γ) on mass transfer. From the figure, it is noticed that the increase in the chemical reaction parameter (γ) causes a decrease in the mass transfer.

Table 2 shows the comparison between the skin friction coefficient $f''(0)$**,** Nusselt number
$\theta'(0)$ and the Sherwood number $\Phi'(0)$ for various values of $\varphi, k, \lambda, Grt, m\ and\ \gamma$ of Damisa and Okedoye (2024). It is observed from the table that the increasing function of the volume fraction (φ) causes a decrease in the skin friction coefficient $f''(0)$, decrease in the Nusselt number
$\theta'(0)$. The increase in the stretching sheet parameter (λ) brings about the decrease in the skin friction coefficient $f''(0)$, decrease in the Nusselt number $\theta'(0)$ and an increase in the Sherwood number (Φ). Also, the increase in the buoyancy due to temperature Grt leads to the increase in the skin friction coefficient $f''(0)$, decrease in the Nusselt number $\theta'(0)$. The increase in the velocity power index (m) yields an increase in the skin friction $f''(0)$ and an increase in the Sherwood number (Φ). Then, the increase in the chemical reaction parameter (γ) causes a decrease in the skin friction coefficient $f''(0)$, an increase in the Nusselt number $\theta'(0)$ and a decrease in the Sherwood number (Φ). All of these results conform with the findings in Damisa and Okedoye (2024). Table 3 shows the results of Skin friction coefficient $f''(0)$, Nusselt number $\theta'(0)$ and the Sherwood number $\Phi'(0)$ for varying values for Buoyancy due to concentration parameter (Gr_c), Radiation parameter (R), second grade fluid parameter (α), Soret Number (Sr) Eckert number (Ec) and the Magnetic parameter, (M) when $Pr = 21.0\ and\ Sc = 0.62$. it is observed from the table that the increase in the buoyancy due to concentration (Gr_c) leads to the increase in the skin friction coefficient $f''(0)$, a decrease in the Nusselt number $\theta'(0)$ and an increase in the Sherwood number $\Phi'(0)$. Also, there is a decrease in the skin friction coefficient $f''(0)$ and the Nusselt number $\theta'(0)$ while an increase in the Sherwood number $\Phi'(0)$ as a result of increase in the radiation parameter (R). On the other hand, there is an increase in the skin friction coefficient $f''(0)$, a decrease in the Nusselt number $\theta'(0)$ and an increase in the Sherwood number $\Phi'(0)$ when there is an increase function of the second-grade parameter (α). The increasing function of the

Soret number (Sr) results in a decrease in the skin friction coefficient $f''(0)$, an increase in the Nusselt number $\theta'(0)$ and a decrease in the Sherwood number $\Phi'(0)$. The increase in the Eckert number (Ec) brings about the increase in the skin friction coefficient $f''(0)$ and the Nusselt number $\theta'(0)$ while the Sherwood number $\Phi'(0)$ decreases. Then the skin friction coefficient $f''(0)$ decreases, the Nusselt number $\theta'(0)$ increases and the Sherwood number $\Phi'(0)$ decreases with an increase in the Magnetic parameter (M).

Table 3: Results of Skin friction coefficient $f''(0)$, Nusselt number $\theta'(0)$ and the Sherwood number $\Phi'(0)$ for varying values for Buoyancy due to concentration parameter(Gr_c), Radiation parameter (R), second grade fluid parameter (α), Soret Number (Sr), Eckert number (Ec) and the Magnetic parameter (M) when $Pr = 21.0\ and\ Sc = 0.62$.

Parameter $(\boldsymbol{Gr, Nb, Nt, Sr, Ec})$	$\boldsymbol{f''(0)}$	$\boldsymbol{\theta'(0)}$	$\boldsymbol{\Phi'(0)}$
$\boldsymbol{Gr_c}$			
0.0	-0.825803	1.26695	-0.68550
1.0	-0.58937	0.91388	-0.67521
2.0	-0.36908	0.72137	-0.67499
$\boldsymbol{R}$			
6.0	-0.77605	1.92677	-0.75169
20.0	-0.78514	0.56042	-0.62713
40.0	-0.78234	0.24168	-0.60000
$\boldsymbol{\alpha}$			
0.1	-0.84725	1.26524	-0.68570
0.3	-0.72902	1.10166	-0.67987
0.5	-0.64502	0.97327	-0.67632
$\boldsymbol{Sr}$			
0.1	-0.65979	1.19531	-0.59709
0.3	-0.66369	1.25136	-0.86813
0.5	-0.66736	1.31607	-1.16699
$\boldsymbol{Ec}$			

0.0	-0.84614	-0.35012	-0.53530
4.0	-0.78257	1.77875	-0.68240
8.0	-0.72741	2.40603	-0.79877
M			
0.0	-0.70277	0.95144	-0.66902
2.0	-1.17647	3.42046	-0.85177
4.0	-1.56536	5.20162	-0.99107

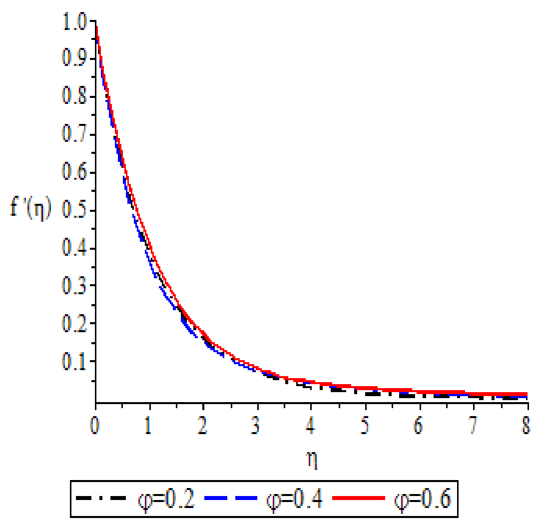

Fig. 2: Impact of volume fraction (φ) on velocity field.

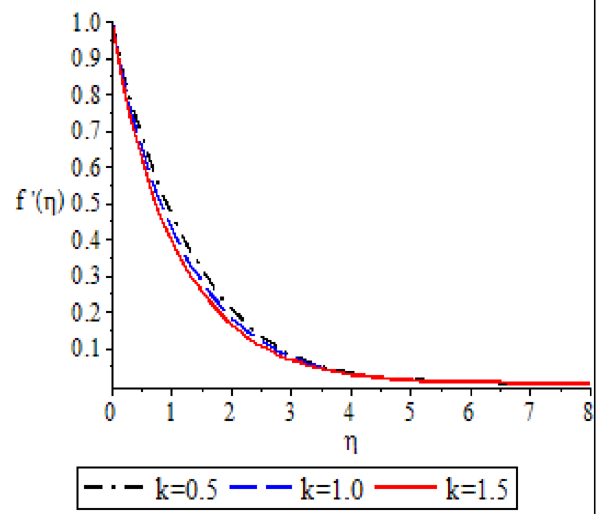

Fig.3: Impact of Porous Medium parameter (k) on velocity Field.

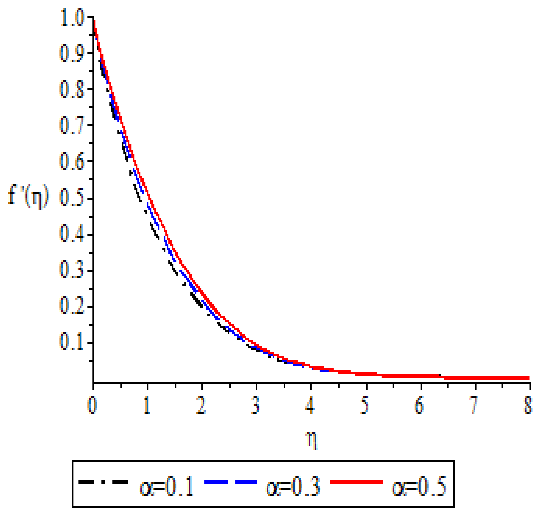

Fig.4: Impact of Second-Grade parameter (α) on velocity field.

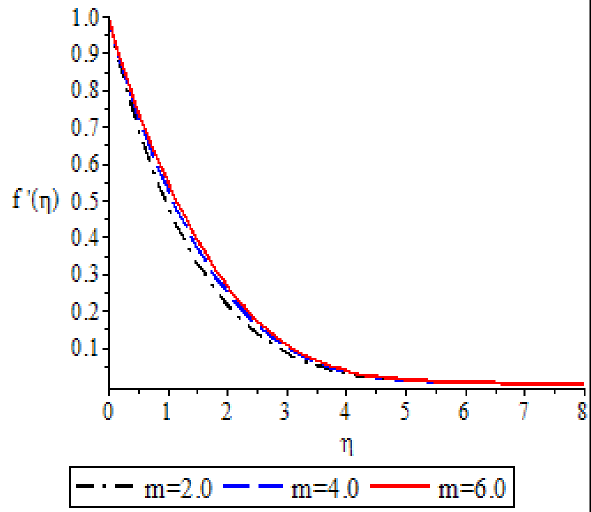

Fig.5: Impact of velocity power Index (m) on velocity field.

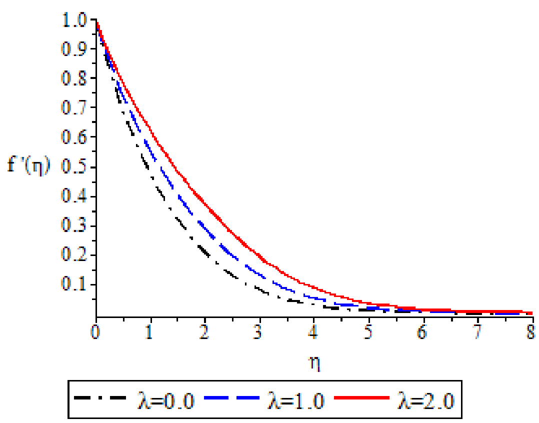

Fig.6: Impact Stretching-sheet parameter (λ) on velocity Field.

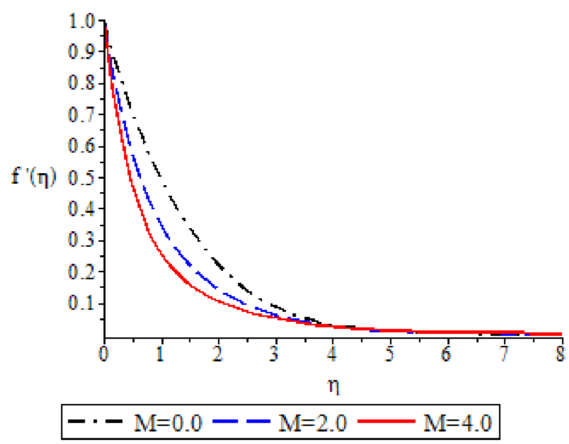

Fig.7: Impact of Magnetic parameter (M) on velocity field.

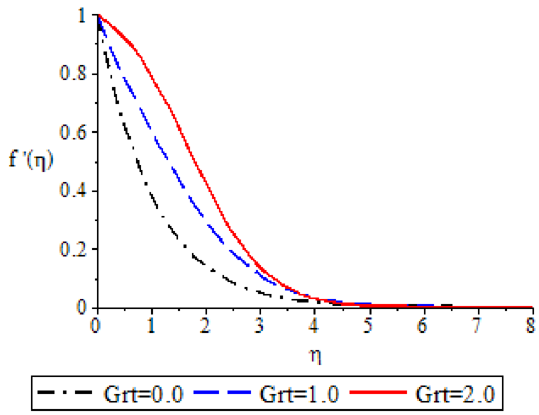

Fig.8: Impact of Buoyancy due to temperature (Fs) on velocity field.

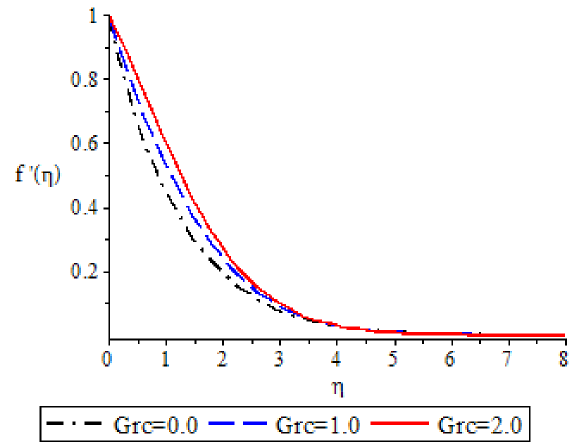

Fig.9: Impact of Buoyancy due to concentration on velocity field.

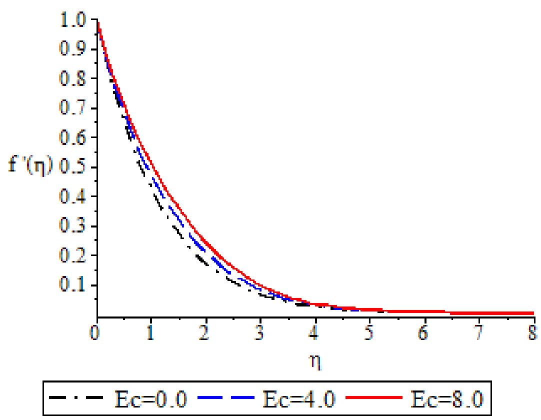

Fig.10: Impact of Eckert number (Ec) on velocity field.

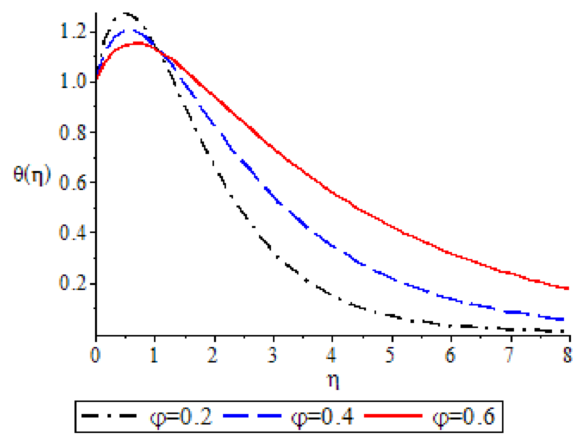

Fig.11: Impact of volume fraction on (φ) on Temperature distribution.

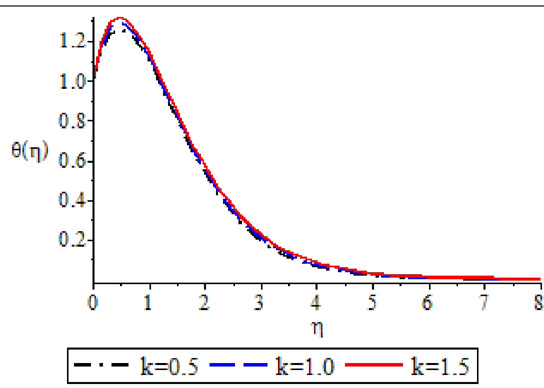

Fig.12: Impact of porous mdium parameter (k) on Temperature distribution.

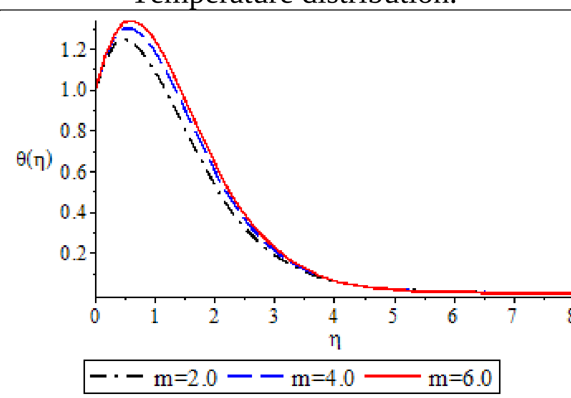

Fig. 13: Impact of velocity power index parameter (m) on Temperature distribution.

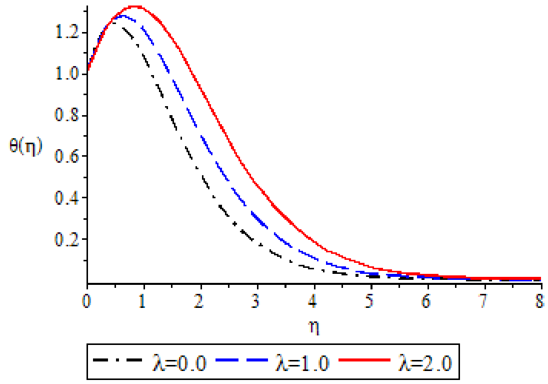

Fig.14: Impact of Stretching-sheet parameter (λ) on Temperature distribution.

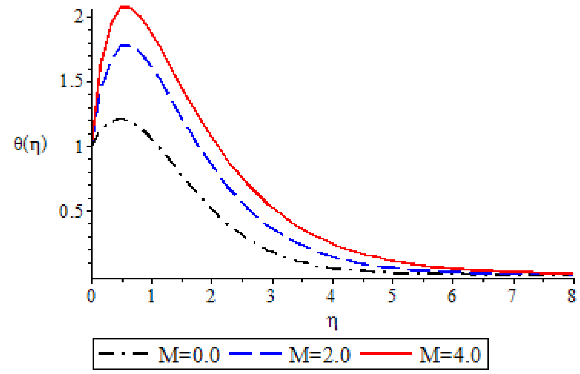

Fig.15: Impact of Magnetic parameter (M) on Temperature distribution.

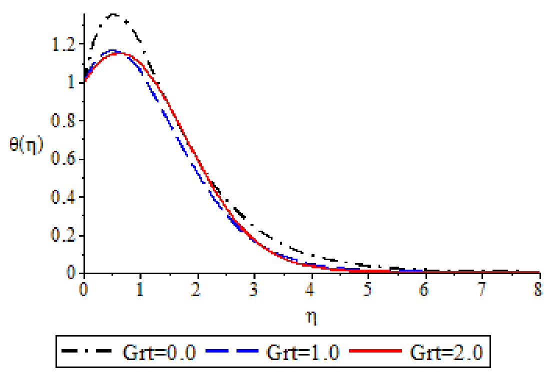

Fig.16: Impact of Buoyancy due to temperature (Grt) on temperature distribution.

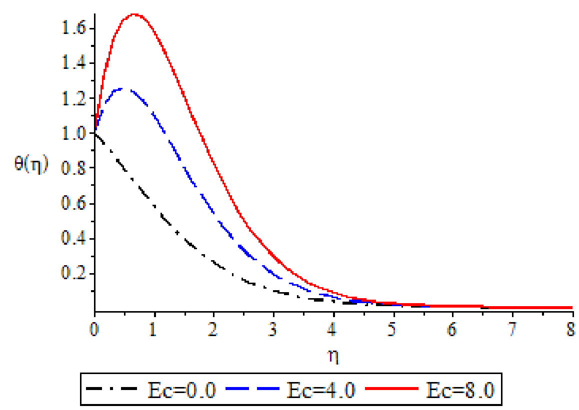

Fig.17: Impact of Eckert number Temperature parameter (Ec) on temperature distribution.

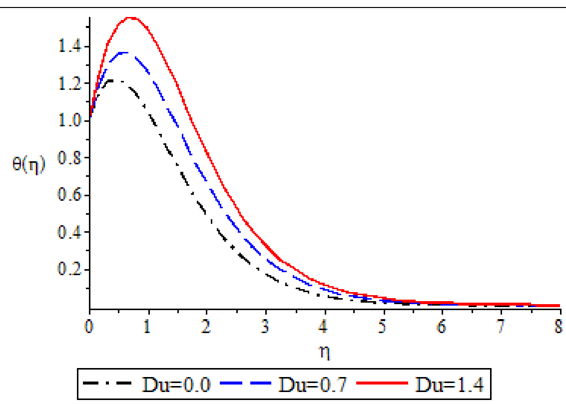

Fig.18: Impact of Dufour number (Du) on Temperature distribution.

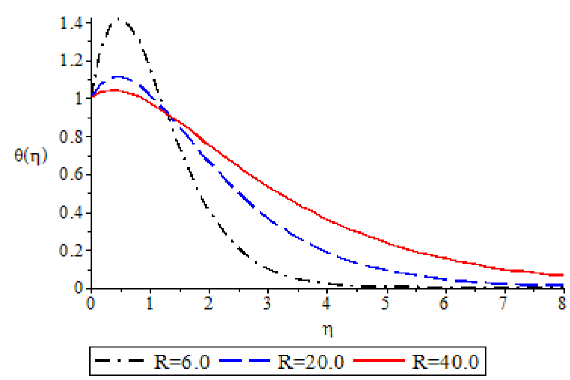

Fig.19: Impact of radiation parameter (R) on temperature distribution.

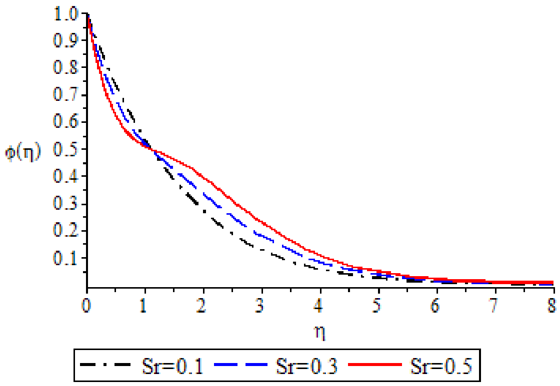

Fig.20: Impact of Soret number (Sr) on Mass transfer distribution.

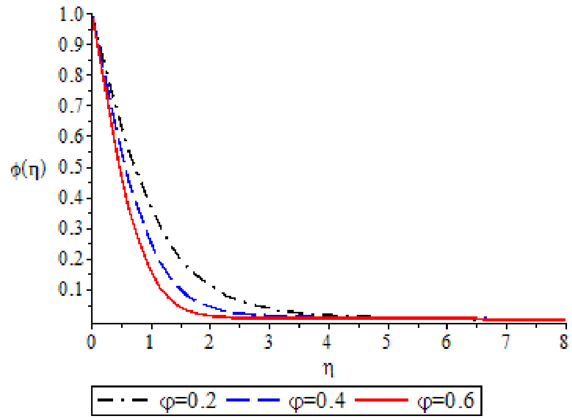

Fig.21: Impact of volume fraction (φ) on Mass transfer distribution.

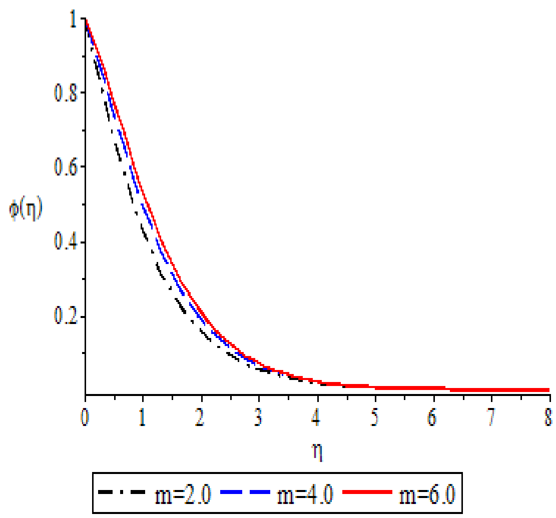

Fig. 22: Impact of velocity power index (m) on Mass transfer distribution.

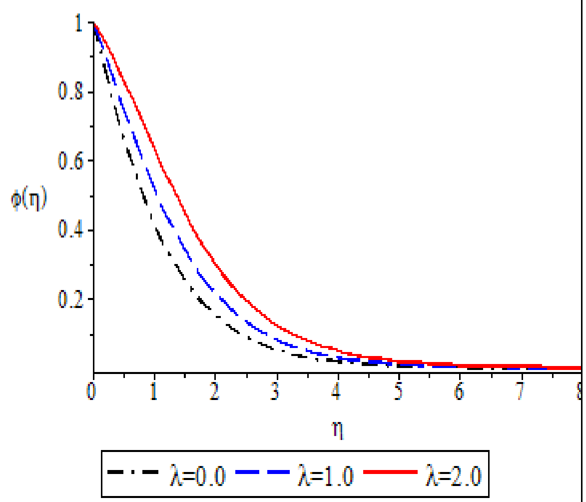

Fig.23: Impact of Stretching-sheet parameter (λ) on Mass Transfer distribution.

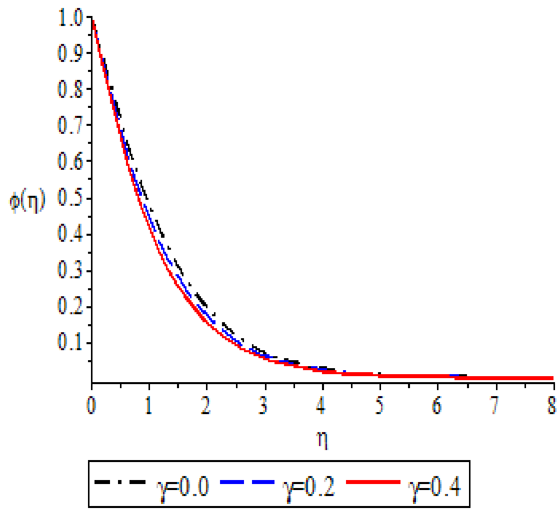

Fig.24: Impact of chemical reaction parameter (γ) on Mass Transfer distribution.

4. CONCLUSION

"Combine effects of buoyancy forces, velocity power index and magnetohydridynamics (MHD) heat and mass transfer of second-grade nanofluid flow over a stretching-porous sheet with chemical reaction" is an article that examined the impact of various parameter on the fluid velocity, temperature, concentration as well as the rate of fluid flow and mass transfer. From the study, the following conclusions were made;

1. The increase in the buoyancy due to temperature leads to the increase in the velocity of the fluid, an increase away from the wall and a decrease at the wall and at the free stream. The increase in the buoyancy due to concentration brings about the increase in the velocity of the fluid.
2. The increase in the velocity power index leads to the increase in the velocity field, temperature distribution and mass transfer of the fluid under consideration.
3. There is a decreasing function of fluid velocity and an increasing function of temperature distribution with the increasing effect in the magnetic parameter.
4. The velocity of the fluid increases with the increasing effects of the second-grade parameter and the increase in the chemical reaction causes a decrease in the mass transfer.
5. The increasing function of the porous medium causes the decrease in the velocity of the fluid flow, an increase in the temperature distribution of the fluid and the increase in the stretching-sheet causes the increase in the fluid velocity, temperature distribution and the mass transfer of the fluid.
6. The increase in the velocity power index yields an increase in the skin friction and an increase in the Sherwood number, the increase in the skin friction coefficient, a decrease in the Nusselt number and an increase in the Sherwood number is caused by the increasing function of the second-

grade parameter (α). Meanwhile, the increase in the buoyancy due to temperature leads to the increase in the skin friction coefficient and a decrease in the Nusselt number.

References

Abbas, Z., Shatanawi, W., and Al-Mdallal, Q. (2023). Nonlinear stretching effects on power-law nanofluid flow: A CFD approach. International Journal of Thermal Sciences, 189, 108234. https://doi.org/10.1016/j.ijthermalsci.2023.108234

Alghamdi, M., Alshomrani, A. S., and Ullah, M. Z. (2023). Dual buoyancy-driven convection in second-grade nanofluids: A numerical study. Journal of Molecular Liquids, 391, 123456. https://doi.org/10.1016/j.molliq.2023.123456

Ali, F., Saqib, M., and Khan, I. (2023). Machine learning-optimized MHD nanofluid flow with heat transfer enhancement. Computers and Fluids, 265, 110003. https://doi.org/10.1016/j.compfluid.2023.110003

Chen, Y., Li, B., and Zhang, X. (2023). Porous media effects on nanofluid flow: A lattice Boltzmann study. Physics of Fluids, 35(7), 072011. https://doi.org/10.1063/5.0157321

Das, S., Chakraborty, S., and Pal, D. (2023). Stretching sheet-induced instabilities in porous media: A CFD investigation. International Journal of Mechanical Sciences, 245, 108112. https://doi.org/10.1016/j.ijmecsci.2023.108112

Gupta, R., and Kumar, S. (2023). Eulerian two-phase modeling of viscoelastic nanofluids: Challenges and solutions. Journal of Non-Newtonian Fluid Mechanics, 312, 104987. https://doi.org/10.1016/j.jnnfm.2023.104987

Ibrahim, W., and Anwar, T. (2023). Exothermic reactions in TiO_2 nanofluids: Stability and mass transfer analysis. Chemical Engineering Science, 278, 118899. https://doi.org/10.1016/j.ces.2023.118899

Khan, U., Ahmed, N., and Mohyud-Din, S. T. (2023). Entropy minimization in Ag-water nanofluids under variable magnetic fields. Energy, 282, 128765. https://doi.org/10.1016/j.energy.2023.128765

Kumar, A., and Pandey, A. K. (2023). Adaptive meshing strategies for non-linear stretching flows. Computers and Mathematics with Applications, 147, 214–230. https://doi.org/10.1016/j.camwa.2023.06.022

Mehmood, R., Rana, S., and Nadeem, S. (2023). MHD effects on Newtonian nanofluid flow over an inclined cylinder. Alexandria Engineering Journal, **75**, 123–135. https://doi.org/10.1016/j.aej.2023.06.045

Nayak, M. K., Mishra, S. R., and Tiwari, A. K. (2023). Fractional derivative modeling of viscoelastic nanofluids in porous media. Applied Mathematics and Computation, 452, 128557. https://doi.org/10.1016/j.amc.2023.128557

Patel, R. V., Joshi, H. C., and Singh, A. K. (2023). Reduced-order modeling of catalytic nanofluid reactions. Industrial and Engineering Chemistry Research, 62(30), 11976–11989. https://doi.org/10.1021/acs.iecr.3c01677

Rana, P., Makinde, O. D., and Chamkha, A. J. (2023). Radiative MHD nanofluid flow with slip effects: Applications in aerospace cooling. Aerospace Science and Technology, 139, 108345. https://doi.org/10.1016/j.ast.2023.108345

Sharma, P., Yadav, D., and Lee, J. (2023). Variable porosity effects on nanoparticle deposition in porous media. Transport in Porous Media, 148(2), 345–367. https://doi.org/10.1007/s11242-023-01954-0

Sheikholeslami, M., Jafaryar, M., and Shafee, A. (2023). Chemical reaction impacts on Al_2O_3-water nanofluid flow in microchannels. Journal of Thermal Analysis and Calorimetry, 148(5), 2013–2025. https://doi.org/10.1007/s10973-023-12151-8

Siddiqui, A. M., Haroon, T., and Raza, N. (2023). Oldroyd-B nanofluid simulations in OpenFOAM: Viscoelastic instabilities. Journal of Computational Physics, 493, 112456. https://doi.org/10.1016/j.jcp.2023.112456

Zhang, L., Wang, H., and Guo, Z. (2023). DNS of anisotropic heat transfer in fibrous porous media. International Journal of Heat and Mass Transfer, 214, 124409. https://doi.org/10.1016/j.ijheatmasstransfer.2023.124409

Ahmed, S. E., and Raizah, Z. (2023). Double-diffusive convection in second-grade nanofluids: A Chebyshev collocation study. ZAMM - Journal of Applied Mathematics and Mechanics, 103(8), e202200287. https://doi.org/10.1002/zamm.202200287

Bég, O. A., Tripathi, D., and Karim, I. (2023). Computational modeling of magneto-nanofluid drug delivery in stenosed arteries. Computer Methods and Programs in Biomedicine, 241, 107765. https://doi.org/10.1016/j.cmpb.2023.107765

Dogonchi, A. S., Waqas, M., and Alghamdi, M. (2023). Entropy generation in radiative Maxwell nanofluid flow with Cattaneo-Christov heat flux. Case Studies in Thermal Engineering, 45, 102989. https://doi.org/10.1016/j.csite.2023.102989

Ghadikolaei, S. S., and Yassari, M. (2023). Nonlinear thermal radiation in MHD TiO_2-Cu/H_2O hybrid nanofluid flow over a stretching sheet. Journal of Magnetism and Magnetic Materials, 587, 171271. https://doi.org/10.1016/j.jmmm.2023.171271

Hayat, T., Qayyum, S., and Alsaedi, A. (2023). Variable thermal conductivity in stagnation points flow of second-grade fluid. International Communications in Heat and Mass Transfer, 148, 107042. https://doi.org/10.1016/j.icheatmasstransfer.2023.107042

Li, Z., Sheikholeslami, M., and Shafee, A. (2023). Heat transfer enhancement in phase change materials using nanoparticles and magnetic fields. Renewable Energy, 216, 119103. https://doi.org10.1016/j.renene.2023.119103

Mahanthesh, B., Mackolil, J., and Job, V. M. (2023). Significance of Marangoni convection in nanofluid flow over a porous stretching sheet. European Journal of Mechanics - B/Fluids, 101, 1–12. https://doi.org/10.1016/j.euromechflu.2023.06.003

Nandi, S., and Kumbhakar, B. (2023). MHD stagnation point flow of Casson nanofluid with chemical reaction and slip effects. Chinese Journal of Physics, 85, 482–496. https://doi.org/10.1016/j.cjph.2023.06.012

Reddy, J. R., Kumar, P. V., and Vajravelu, K. (2023). Nonlinear convection in second-grade nanofluids: A stability analysis. Communications in Nonlinear Science and Numerical Simulation, 126, 107490. https://doi.org/10.1016/j.cnsns.2023.107490

Sajid, T., Jamshed, W., and Eid, M. R. (2023). Solar radiation effects on Cu-TiO_2/H_2O hybrid nanofluid flow over a permeable stretching sheet. Solar Energy, 262, 111836. https://doi.org/10.1016/j.solener.2023.111836

Tlili, I., Khan, W. A., and Ramadan, K. M. (2023). Thermal performance of radiative hybrid nanofluids in microchannel heat sinks. International Journal of Thermal Sciences, 192, 108411. https://doi.org/10.1016/j.ijthermalsci.2023.108411

Wakif, A., Boulahia, Z., and Animasaun, I. L. (2023). Significance of Coriolis forces on rotating nanofluid flows: A comparative CFD study. European Physical Journal Plus, 138(8), 697. https://doi.org/10.1140/epjp/s13360-023-04316-3

Zaib, A., Rashidi, M. M., and Bhattacharyya, K. (2023). Dual solutions of MHD nanofluid flow over an exponentially shrinking sheet with radiation. Journal of Nanofluids, 12(4), 1141–1148. https://doi.org/10.1166/jon.2023.1999

Nomenclature

Parameter	Definition		Parameter	Definition
$\boldsymbol{Ec}$	Eckert number		$\boldsymbol{A}$	Area of emitting body of temperature
$\boldsymbol{Grt}$	Buoyancy coefficient factor		$\boldsymbol{l}$	Characteristics length
$\boldsymbol{S_G}$	Ratio of Nanofluid particle and base fluid		$\boldsymbol{T_\infty}$	Ambient temperature
$\boldsymbol{R_d}$	Thermal radiation parameter		$\boldsymbol{C_\infty}$	Ambient concentration
$\boldsymbol{Sc}$	Schmidt number		η	similarity variable
$\boldsymbol{D_1}$			Pr	Prandtl number
$\boldsymbol{Sr}$	Soret number		γ	Scaled chemical reaction parameter
$\boldsymbol{B}$	Area of emitting body of concentration		k_1	Porous medium parameter
$\boldsymbol{T_w}$	wall temperature		M	magnetic parameter
$\boldsymbol{C_w}$	Wall concentration		Sr	Soret number
$\boldsymbol{Du}$	Dufour number		Sc	Schmidt number
$\boldsymbol{k_1}$	Porous medium parameter		R_d	Radiation parameter
$\boldsymbol{Grc}$	Buoyancy coefficient ratio		Ec	Eckert number
$\boldsymbol{R}$	Thermal radiation parameter		Grt	coefficient respectively
$\boldsymbol{k_{nf}}$	Thermal conductivity of Nanofluid		τ_w	the *shear stress* at the surface
			q_w	*heat flux* at the surface
$\boldsymbol{D_m}$	Mass diffusivity		J_w	*mass flux* at the surface